JOURNAL OF GEOPHYSICAL RESEARCH, VOL. 115, B06308, doi:10.1029/2009JB006608, 2010

A broad 660 km discontinuity beneath northeast China revealed by dense regional seismic networks in China

Baoshan Wang[1,2] and Fenglin Niu[1]

Received 12 May 2009; revised 5 November 2009; accepted 14 January 2010; published 15 June 2010.

[1] We examined the P wave velocity structure around the 660 km discontinuity at the tip of the subducting Pacific slab beneath northeastern China by forward modeling waveform triplication data. A total of 742 broadband seismograms were recorded by dense regional seismic networks in China from a deep earthquake that occurred near the border of east Russia and northeast China, providing an unprecedented density of ray coverage near the front edge of the subducting Pacific slab. Multiple P waves were observed on single seismograms in the distance range of ~14°–29°. The P wave triplication shows the following two features: (1) the direct arrival traveling above the 660 km discontinuity (AB branch) extends as far as ~29°, approximately 6° further than the prediction from velocity model of International Association of Seismology and the Physics of the earth's interior (iasp91); (2) the refracted wave propagating through the lower mantle (CD branch) appears at a distance a few degrees greater than that of the iasp91 synthetics. Forward waveform modeling suggests that they are best explained by a high-velocity transition zone underlain by a ~50–70 km thick 660 km discontinuity. The broadened discontinuity is likely caused by multiple phase transitions associated with the dissolutions of olivine and garnet components.

Citation: Wang, B., and F. Niu (2010), A broad 660 km discontinuity beneath northeast China revealed by dense regional seismic networks in China, *J. Geophys. Res.*, *115*, B06308, doi:10.1029/2009JB006608.

1. Introduction

[2] The 660 km seismic discontinuity is generally believed to be caused by a phase change of the primary constituent of the upper mantle, the γ-olivine or ringwoodite [*Ito and Takahashi*, 1989]. At the approximate pressure-temperature conditions occurring at a depth of 660 km, the γ-olivine, transforms into perovskite $(Mg,Fe)SiO_3$ plus magnesiowüstite (Mg,Fe)O. The phase transition (also known as the post-spinel transformation) is observed to occur within a relatively narrow pressure range, consistent with the seismic observations that the 660 km appears to be sharp. At low-temperature condition, the post-spinel transformation tends to occur at high-pressure conditions [e.g., *Ito and Takahashi*, 1989]. This is also consistent with seismic observations of a depressed 660 km in the subduction regions [e.g., *Shearer and Masters*, 1992; *Vidale and Benz*, 1992; *Wicks and Richards*, 1993; *Niu and Kawakatsu*, 1995; *Collier and Helffrich*, 1997; *Flanagan and Shearer*, 1998; *Niu et al.*, 2005; *Li et al.*, 2008].

[3] The nonolivine minerals, on the other hand, undergo a series of transformations in the depth range of ~600–750 km that result in velocity changes in, more or less, a gradual way. The mineral phases and the associated transitions appear to strongly depend on temperature. *Vacher et al.* [1998] calculated the seismic velocity profiles with pyrolite and piclogite assemblages and found that at low-temperature conditions the phase transitions of the nonolivine minerals can produce sharp velocity increases, resulting in a multiple-step transition from the upper to lower mantle. *Niu and Kawakatsu* [1996] observed multiple *P* to *S* conversions between 660 and 780 km recorded by the Global Seismic Network (GSN) station MDJ (Mudanjiang) in northeast China. The conversion points are located within the subducting Pacific lithosphere. This multiple-discontinuity structure was further confirmed by *Ai et al.* [2003] with a small-scale broadband array. *Ai et al.* [2003] also found the regions with multiple seismic discontinuities are intermittently distributed. They are mixed with regions with a simple depressed 660 km discontinuity, which suggests that the phase diagrams of the nonolivine minerals are extremely sensitive to temperature, as shown in the calculation of *Vacher et al.* [1998]. With the same array data, *Li and Yuan* [2003], on the other hand, found a single but deeper-than-normal 660 km discontinuity in the entire region. The discrepancy may result from different data bandwidths used in these studies, as shown in *Niu and Kawakatsu* [1996]. Independent seismic observations using other techniques thus become crucial in order to confirm whether a complicated 660 km is the true feature in the region before we further explore its mineral physical and dynamical implications.

[1]Department of Earth Science, Rice University, Houston, Texas, USA.
[2]Also at Institute of Geophysics, China Earthquake Administration, Beijing, China.

0148-0227/10/2009JB006608

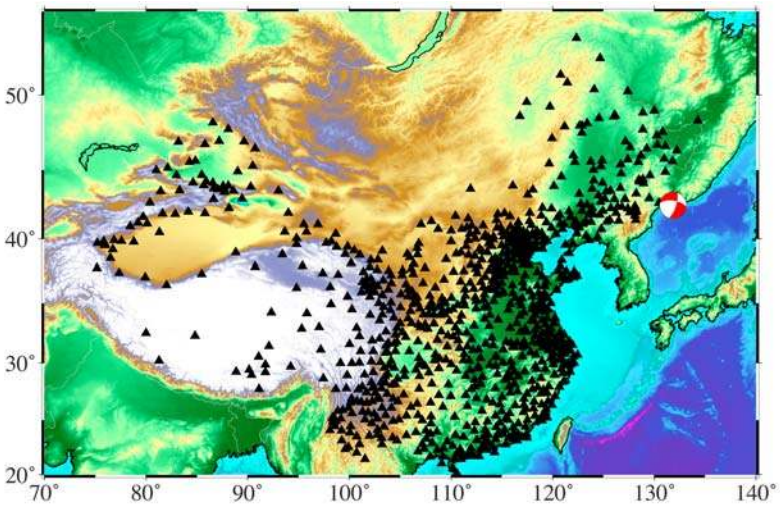

Figure 1. Map showing the stations of the national and regional networks operated by the China Earthquake Administration (solid triangles). Also shown is the focal mechanism of the deep earthquake used in this study (beach ball).

[4] Forward modeling of the multiple *P* and *S* waves (triplicated waves) observed on single seismograms recorded in the distances <30° has been widely used to investigate the seismic structure around the 660 km discontinuity. As the multiple waves recorded in a single station have very similar raypaths near the source and the receiver, the relative waveforms are not subjected to potential distortions from the unmodeled heterogeneities in the crust and the uppermost mantle. *Tajima and Grand* [1995, 1998] used the multiple P wave arrivals recorded by China Digital Seismograph Network (CDSN) stations from regional deep focus earthquakes and found high-velocity anomalies within the transition zone beneath the northwestern Pacific subduction zones. *Brudzinski and Chen* [2000, 2003] used similar observations to map out anomalous mantle velocities in the transition zone associated with the Tonga-Fiji subduction zone. More recently, *Wang et al.* [2006] and *Wang and Chen* [2009] investigated both the *P*- and *S*-wave triplications recorded by the expanded CDSN and temporal arrays and found large velocity variations beneath the region.

[5] In this study, we used more than 650 broadband recordings of the regional seismic networks in China from a deep earthquake occurring at the offshore of the east Russia-northeast China border (Figure 1) to study the transition zone structure near the front edge of the Wadati-Benioff zone of the subducted Pacific slab [*Fukao et al.*, 1992, 2001]. The unprecedented ray coverage allowed us to constrain some first-order features of the upper-lower mantle boundary in this well-studied region.

2. Forward Waveform Modeling with CEArray Data

2.1. Waveform Triplication Induced by a Seismic Discontinuity

[6] Teleseismic tomography has excellent horizontal resolution, but the depth resolution is often less than ideal. On the other hand, the triplicated waves observed on single seismograms can put important constraints on radial velocity variations with depth. As shown in Figure 2a, from a deep focus earthquake one would expect to observe multiple waves that propagate through different parts of the mantle at a single station when a rapid velocity change (seismic discontinuity) is present below the source. These waves include the direct arrival that travels above the seismic discontinuity, the waves reflected and refracted at the discontinuity (Figure 2a). In Figure 2b, we show the travel times of these three phases: the direct arrival (AB branch), the reflected phase (BC branch), and the refracted phase (CD branch) in the distance range of 12° to 32° calculated from the iasp91 model [*Kennett and Engdahl*, 1991] for a 520 km deep earthquake. As noted in section 1, the direct and refracted waves share nearly the same raypaths in the uppermost mantle, so the relative moveouts between these two phases are very sensitive to seismic structure immediately above and below the 660-km discontinuity [*Tajima and Grand*, 1995, 1998; *Brudzinski and Chen*, 2000, 2003; *Wang et al.*, 2006; *Wang and Chen*, 2009].

2.2. CEArray Records from a Deep Focus Earthquake

[7] In this study we used the waveform data collected by the national and regional seismic networks in China. To better monitor the seismic activity in the Mainland China, the China Earthquake Administration (CEA) has gradually upgraded and expanded its national and regional networks since the late 1990s. Currently, CEA owns the largest permanent seismic network in the world, which consists of 32 regional networks with more than 1000 stations (Figure 1) including 850+ broadband stations [*Zheng et al.*, 2009]. The seismometers are a combination of STS2, GURALP3T, GURALP3ESP, KS2000 and Chinese national broadband sensors JCZ-1 (360 s to 50 Hz), CTS-1 (120 s to 50 Hz), FBS-3 (20 s to 20 Hz), and some other types of sensors. The 1000+ stations formed a large two-dimensional areal array with an aperture ~6700 km from east to west and ~3500 km from north to south. For the remainder of this paper, we will refer to these stations as the CEArray. Station spacing varies

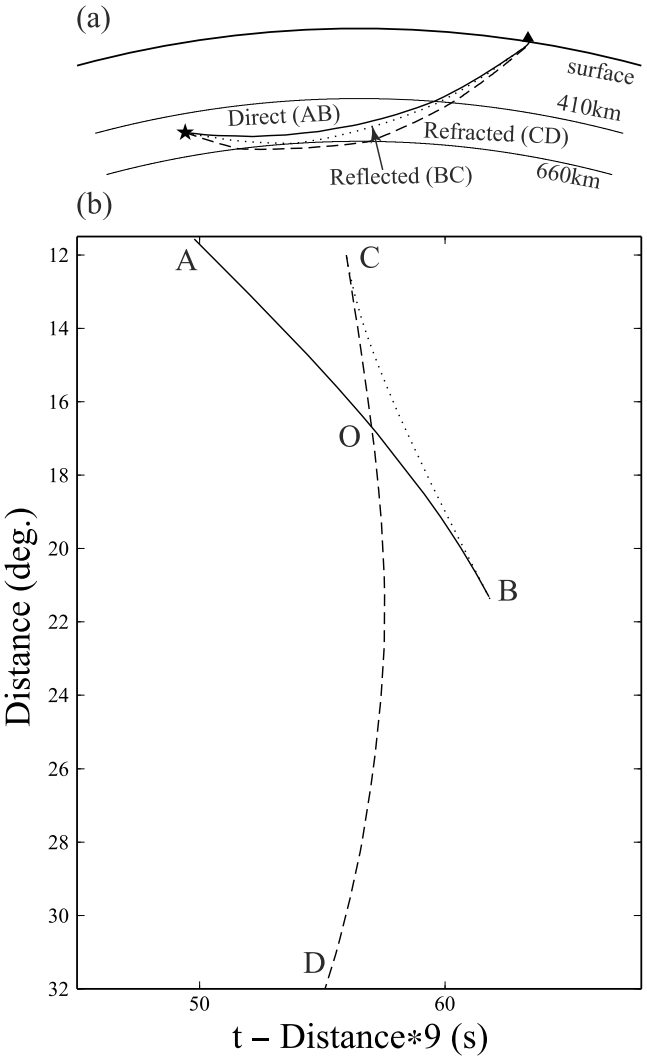

Figure 2. Schematic raypaths of the multiple arrivals (a) and the calculated travel times of these arrivals (b). A 520 km deep source and the iasp91 model were used in calculating the travel times. The direct AB phase, the reflected BC phase, and the refracted CD phase are shown in solid, dotted, and dashed lines, respectively.

drastically with location and reaches to ~50–100 km in the eastern and central parts of China.

[8] A moderate-sized (M_w 5.7) deep focus earthquake (513 km, US Geological survey Preliminary Determinations of Epicenters, PDE catalog) occurred at the offshore near the border between east Russia and northeast China (Figure 1) on 19 May 2008 (origin time: 10:08:36.3 UTC; epicenter: 42.503°N, 131.872°E, PDE catalog). This earthquake was recorded by 742 CEArray broadband stations in a distance range between 1° and 43°. We chose a total of 685 recordings in the distance range of 5°–35° that covers the entire triplication to investigate velocity changes across the upper-to-lower mantle transition as well as lateral variations within and around the subducting Pacific slab. We selected the earthquake for two reasons: (1) the deep M 5.7 earthquake has a very simple source time function and yet it generated seismic waves strong enough to be recorded by the entire CEArray; (2) this event occurred below the 410 km discontinuity, so we don't need to worry about the potential waveform complication resulting from this discontinuity. Using a large amount of records from a single source also allows us to avoid complication resulting from changes in the source waveform.

[9] We first removed the instrument response from each seismogram, and then filtered it with a band-pass filter between 20 s and 6 Hz. The preprocessed velocity records were further integrated into displacement data. Most of the CEArray stations are clustered within the azimuth range between 222° and 270° (Figure 1). To map lateral velocity variations, we sorted the seismograms by station azimuth. A 5° azimuth bin was used to group the seismograms. For each bin group, we first plotted the seismograms in the order of epicentral distance and then manually picked the AB and CD arrivals by tracking the relative moveouts of the two phases. These travels times were further plotted as a function of epicentral distance. We used this plot to identify variations in the AB and CD waveforms and finally divided the waveform records into three groups, corresponding to three azimuthal ranges from 222° to 240°, 240° to 255°, and 255° to 270°, respectively. Hereafter we refer them as subregions A, B, and C, respectively. In Figure 3, we plotted the differential travel times between AB and CD measured from the three subregions as a function of epicentral distance. There are some variations in the AB-CD differential times in each azimuth range, which may be related to the complicated slab geometry in the region. The difference between subregions B and C appears to be rather small, but they are significantly different from subregion A. The AB-CD differential times measured from subregions B and C are systematically larger those estimated from

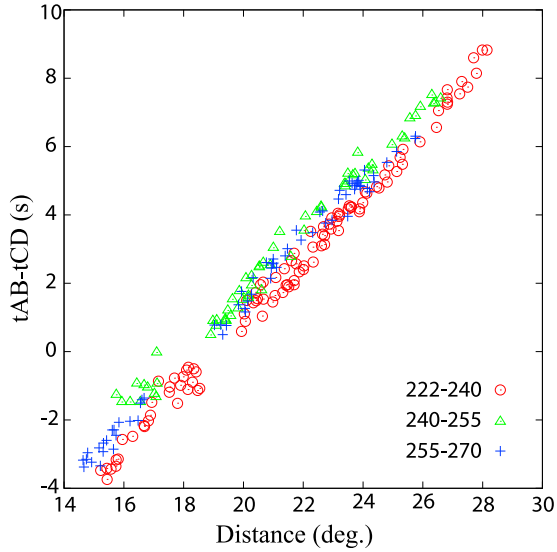

Figure 3. Observed relative travel time between the direct (AB) and the refracted (CD) phase in three subregions are plotted as a function of epicentral distance. The differential times in subregions B and C are approximately 1 s larger than those in subregion A across the entire distance range, which reflects a systematic structural change among different subregions.

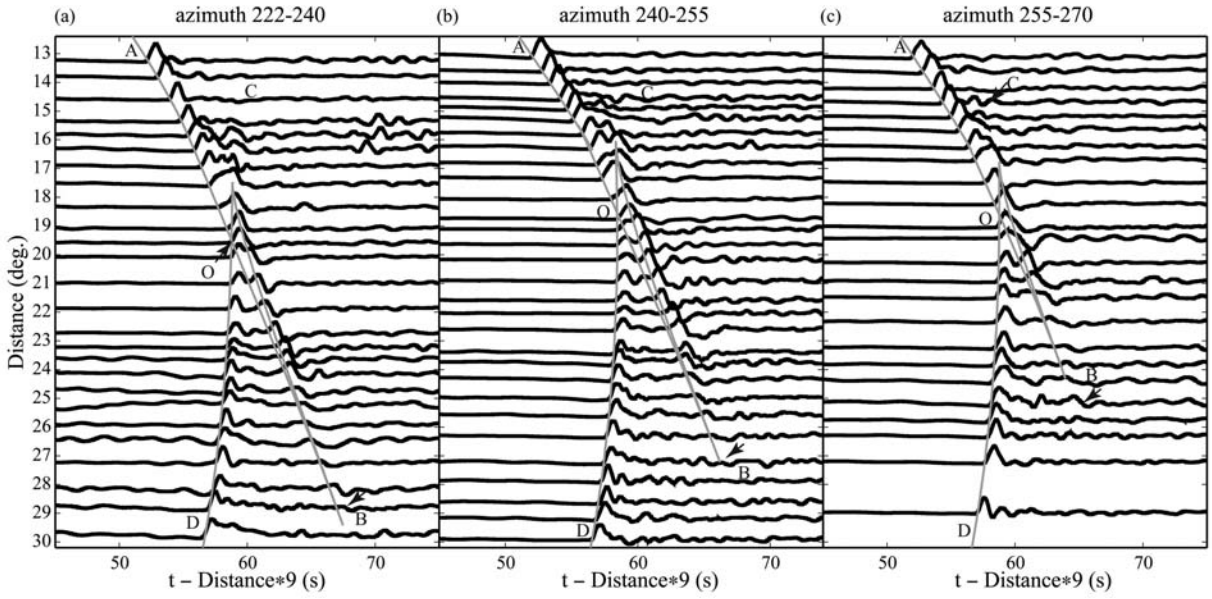

Figure 4. Record sections for three different azimuth ranges, (a) subregion A: 222°–240°, (b) subregion B: 240°–255°, and (c) subregion C: 255°–270°. For display purpose, only a small portion of the seismograms is shown here. The ray-theory-based travel times, predicted from our best-fitting models shown in Figure 8, are plotted in shaded lines. Note here we adjusted the first arrival times of the data in order to align the observed first arrivals with the model predictions. The adjustments are very minor, usually less than 0.5 s.

subregion A, suggesting that significant lateral variations in velocity structure near the 660 km discontinuity exist in the study region.

2.3. Major Features Observed in the P Wave Triplication

[10] Subsets of waveforms from the three subregions are shown in Figure 4. The three recording sections show the following unique features: (1) the CD phase refracted at the 660 km discontinuity does not show up until ~14°–15° away from the earthquake, while the iasp91 synthetics show a C cusp distance of as close as ~7° (Figure 5); (2) the AB branch sampling the lowermost upper mantle (the B cusp) extends to as far as ~29° for subregion A, ~27° for subregion B, and ~25° for subregion C, respectively. All are located at much higher epicentral distance than the iasp91 prediction (Figures 2 and 5); (3) the crossover of the AB and CD branches of the three sections occurs between 19° and 20°, a few degrees further than the iasp91 prediction (Figures 2 and 5).

2.4. Constraints on P Wave Velocity Models

[11] In general, the slopes of AB and CD branches are determined, respectively, by the velocity gradients above and below the 660 km discontinuity. The terminal distance of the direct AB phase (i.e., the location of the B-cusp) is sensitive to the velocity gradient immediately above the 660 km discontinuity, while the emerging distance of the C cusp of the refracted CD branch depends largely on the velocity changes immediately below the discontinuity. The crossover distance of the AB and CD branches, on the other hand, is closely related to the amplitude of the velocity jump across the discontinuity.

[12] To better illustrate how velocity structure above and below the discontinuity affects the triplication, we show synthetic seismograms from two modified iasp91 models in Figures 5 and 6. The modified velocity model shown in Figure 5b has a high-velocity layer with a very low gradient at the lowermost upper mantle, which approximates a subducted cold lithosphere lying above the 660 km discontinuity. This model predicts an extended AB branch with a terminal distance of approximately 27° (B′ in Figure 5a) in contrast to the iasp91 project featuring by a fast-dying AB (B in Figure 5a). The high-velocity layer also changes the relative moveout between AB and CD after the crossover distance.

[13] Recall that the initial point of the refracted CD branch is mainly constrained by the velocity gradient at the top of the lower mantle. In principle, the thickness of the 660 km discontinuity is a measure of this gradient. The iasp91 model has a first-order (0 km thick) 660 km, resulting in an infinite gradient. Such an infinite gradient is actually the most effective way to bend the refracted waves, leading to an extended CD branch with the C cusp occurring at a short epicentral distance. For comparison, we created a second model that has the same velocity structure as the iasp91 model except for a broad discontinuity between 660 and 720 km (Figure 6b). Synthetic seismograms from this model and the iasp91 are shown together in Figure 6a for comparison, the travel time curves based on ray theory calculated with the TauP method [*Buland and Chapman*, 1983] are shown in the inset of Figure 6b. The CD phase of the model with a broad discontinuity starts to appear at ~14° on the synthetic seismograms (C′ in Figure 6a), while it shows at much a shorter distance on the iasp91 synthetics (C in

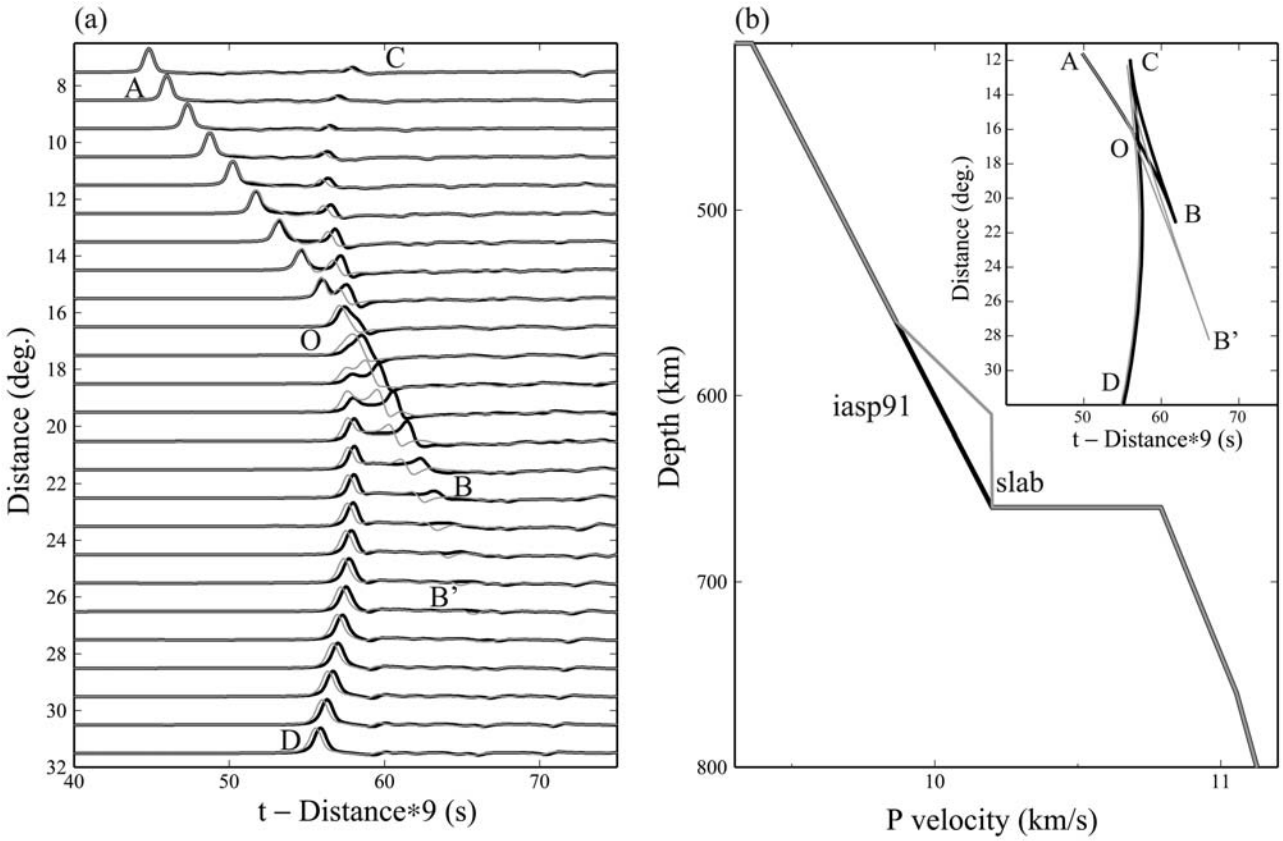

Figure 5. (a) Waveforms calculated from (b) two velocity models: the iasp91 model (dark line) and the high-velocity slab model (shaded line). The slab model is modified from iasp91, and has a high-velocity layer with a very low gradient right above the 660 km. This low gradient layer extends the AB branch to a longer distance. Inset in Figure 5b shows travel times calculated from these two velocity models.

Figure 6a). The same feature is also observed in the travel time curves (Figure 6b inset).

[14] Our observations with a far-reaching AB branch and a shortened CD branch require a combination of these two types of models. In the next section, we will follow this direction and extensively explore the model space to find models that can best explain the observed triplication data.

3. Forward Modeling

[15] To model the velocity structure around the 660 km, we took two iterative steps using trial and error. The first step involves computing ray theory based travel times for the three phases. This was done with the TauP method proposed by *Buland and Chapman* [1983]. In this stage, the model is judged by comparing the predicted travel time curves with the observed slopes of AB and CD branches and the differential travel times between the two phases. In general, the average velocity above and below the 660 km discontinuity can be well constrained by travel time fitting. Once a model passed the first stage, we moved to the second step (i.e., waveform modeling). We first used the model to calculate the synthetic seismograms with the reflectivity code developed by *Wang* [1999]. We then manually compared and contrasted the observed and synthetic waveforms. As stated in section 2, the waveform data are the instrument-response removal and band-pass filtered displacement records. We only accept models that explain both the observed travel times (including the differential travel times of the two phases) and waveform amplitudes. As previously mentioned, since AB and CD phases share similar raypaths in the shallow part of the mantle, the triplicated waveforms have little resolution on velocity structure above the earthquake. We thus fixed the velocity structure above the source in searching for the best-fitting models for the three subregions. More specifically, the velocity profile above the source was taken from the iasp91 model, and large perturbations were allowed only for the lower transition zone and the uppermost lower mantle. Also we tried to keep the velocity models as simple as possible.

[16] The uncertainty in the earthquake location, especially the focal depth, may affect the fitting between the predictions and observations. To minimize this uncertainty, we relocated the earthquake with broadband seismograms recorded by the GSN and other global seismic networks collected by the Incorporated Research Institute for Seismology (IRIS). We manually picked the P and pP arrival times from 230 stations located in teleseismic distances (with epicenter distance 30°–90°). We fixed the epicenter and conducted a grid search to find the focal depth that best explains the observed differential pP-P travel times. We used iasp91 model to compute the predicted pP-P times. As our models have the same velocity profile as the iasp91 model above the source, these predictions are expected to be same if our final models

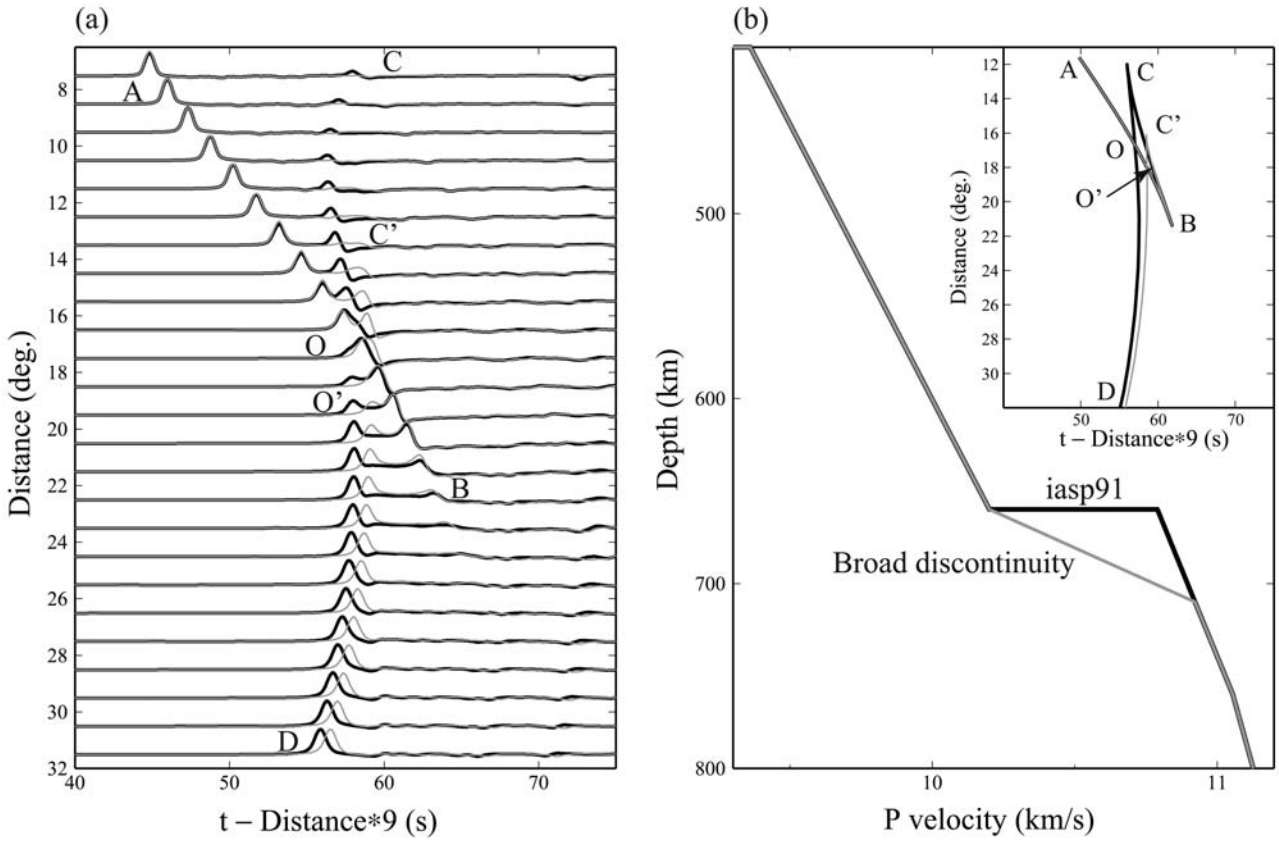

Figure 6. (a) Waveforms calculated from two velocity models: the iasp91 model (dark line) and the broad 660-km model (shaded line). The latter has a 60 km thick 660 km that extends from 660 to 720 km deep. The broad discontinuity model predicts a delayed occurrence of the C cusp (C′ in Figures 6a and 6b inset.) Inset in Figure 6b shows travel times calculated from these two velocity models.

are used. The misfit of differential pP-P times reaches a minimum at the depth of 520 km (Figure 7). The minimum differential time residual is 0.07 s with a standard deviation of 0.32 s that translates to a 2 km uncertainty in the relocated depth (Figure 7). The corresponding uncertainty in the C cusp distance is less than 0.1°. We used a focal depth as 520 km and the Harvard Centroid Movement Tensor (CMT) solution in computing the synthetics.

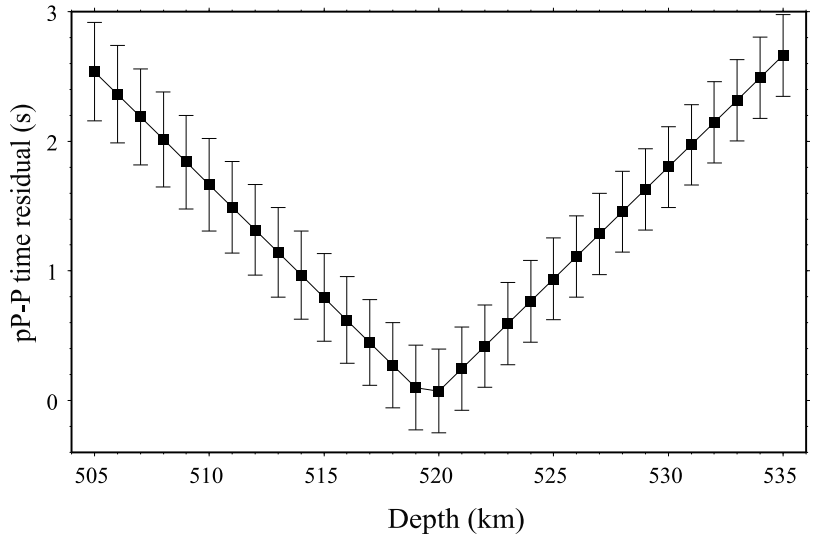

Figure 7. pP-P differential time residuals with respect to the iasp91 model are shown as a function of assumed hypocentral depth.

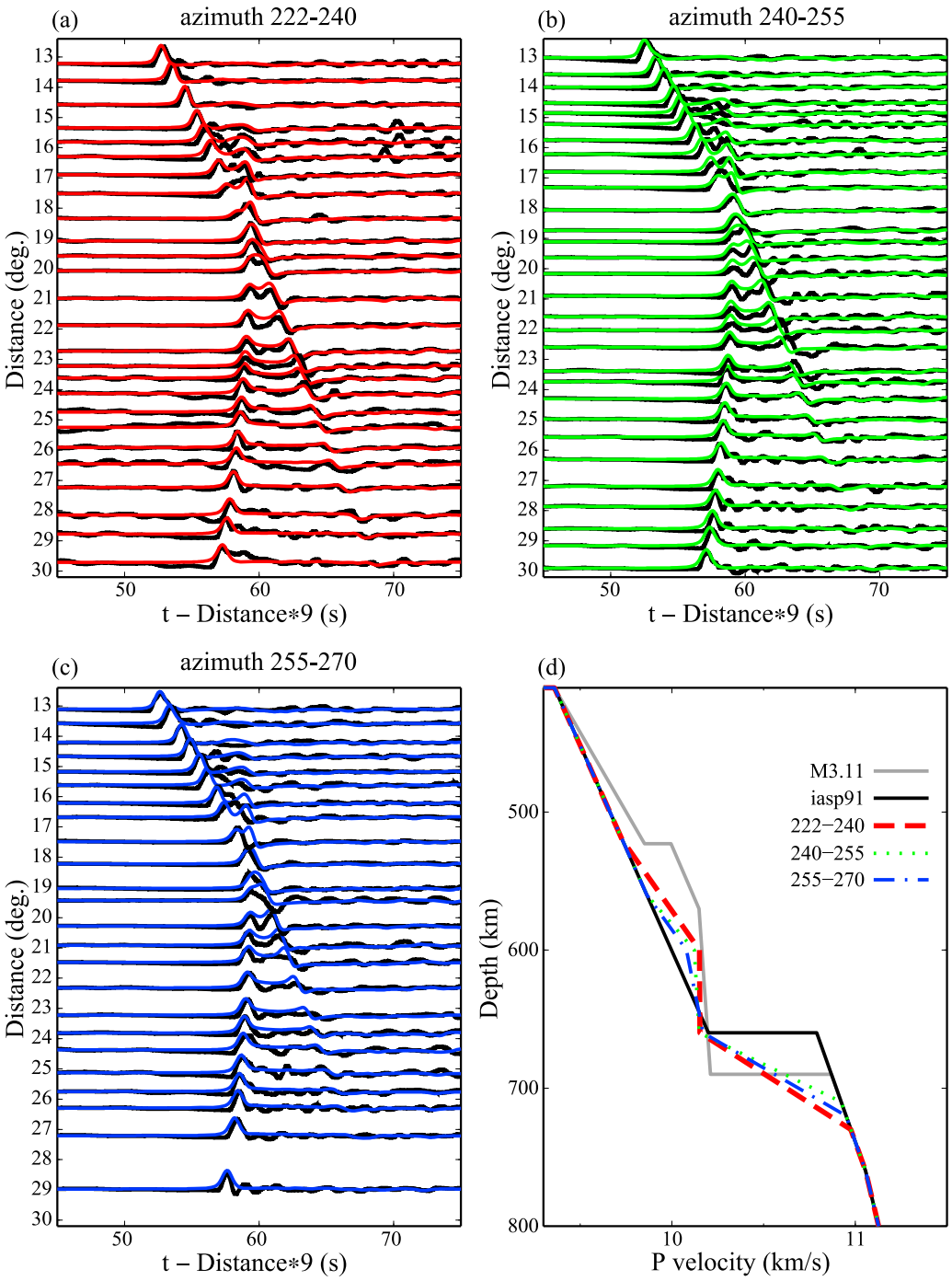

Figure 8. Synthetic waveforms (colored) computed from velocity models shown in (d) are shown together with the observed waveforms (black): (a) subregion A with an azimuth range of 222°–240° (red), (b) subregion B in azimuths between 240° and 255° (green), and (c) subregion C with azimuths coverage of 255°–270° (blue). Observations were aligned with synthetics at the first arrivals. Note the excellent match between the synthetics and the observed waveforms. The velocity model corresponding to subregions A, B, and C are shown in red dashed, green dotted, and blue dash-dotted lines, respectively. The M3.11 and iasp91 models are shown in gray and black, respectively.

[17] We must emphasize here that we are trying to fit the relative moveout of the AB and CD phases, rather than the absolute arrival times of the two phases. To do this we manually aligned the picked first arrivals with the synthetic first arrivals. Differences between the observed and calculated first arrival times from the final models are less than 0.5 s and are considered to be due to unmodeled anomalies at shallow depths right beneath individual stations. We extensively explored the model space and obtained the best-fitting velocity models for the three recording sections. The

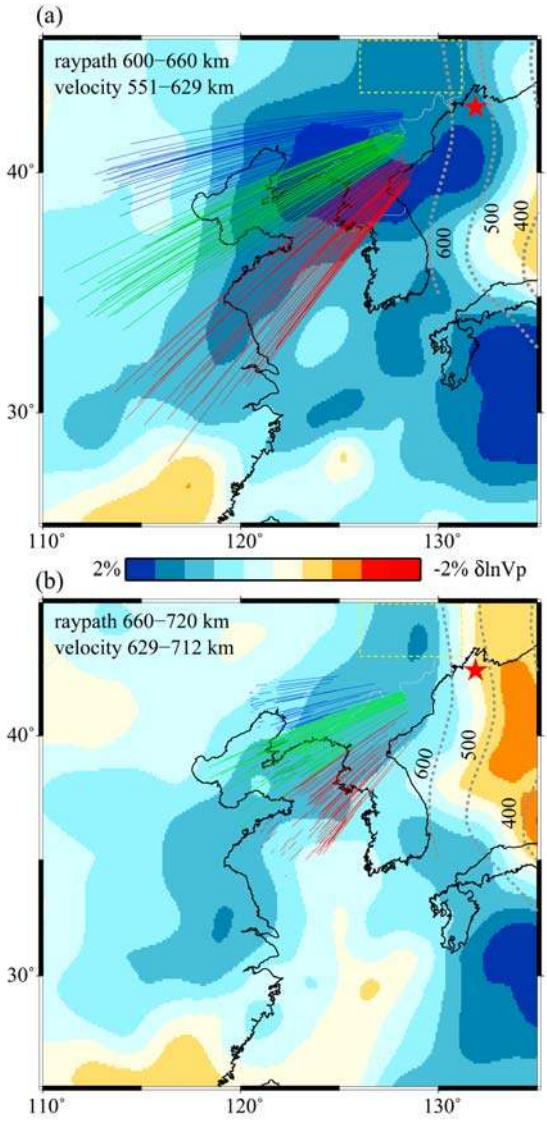

Figure 9. Raypaths plotted on top of tomographic images of *Fukao et al.* [2001] for (a) AB and (b) CD. Raypaths in subregions A, B, and C are shown in red, green, and blue lines, respectively. Star indicates the earthquake, and the dashed lines represent the Wadati-Benioff zone of the subducting Pacific slab. Region with a multiple-discontinuity structure identified by *Ai et al.* [2003] is indicated by the rectangle in yellow dashed lines.

best-fitting models and their corresponding synthetics are shown in Figure 8. Note that since we have no constraint on the shallow part of the models, we removed the travel time differences between the observed and the predicted first arrivals, which are usually less than 0.5 s, in plotting the synthetic and observed records in Figures 4 and 8. In general, the synthetic records calculated from these rather simple models match reasonably well with the observed waveforms. It is highly likely that the true velocity structures beneath the three subregions are more complicated because we noticed that there are some misfits at some distances; for example, at around 23° all the synthetics in the three sections underpredict the differential times of the two phases. We also noticed that overall the fitting of the subregion A is slightly better than the other two subregions. In subregion C, the calculated CD phase tends to arrive later than the observed one in the distance range of 16°~17.5°, resulting a large misfit.

4. Results and Discussion

[18] The final velocity models of the three subregions shown in Figure 8d share some similar features. Immediately below the source, a high-velocity layer with a high gradient extends from 520 to 600 km. The high gradient might be an artifact since we fixed the velocity structure about the source. Also constraints on the velocity structure above 600 km come mainly from travel time curve of the AB phase before 16°, where the refracted CD phase is not available. The velocity structure between 520 and 600 km is thus less well constrained than those below it. We noticed that the high-gradient layer in subregions B and C starts at around 560 km, which is different from the 520 km of the model A. This difference could also be an artifact. The layer below this high-gradient layer has an almost constant velocity, which, as mentioned previously, we believe is well constrained. Models from *Tajima and Grand* [1995] and *Wang and Chen* [2009] are also featured by this low-gradient, high-velocity structure at the base of the upper mantle. Since velocity above this layer is less well constrained, it is possible that this low-gradient layer starts at a depth shallower than 600 km, like the M3.11 [*Tajima and Grand*, 1998] model does. The peak anomaly in the three models all occurs at around 600 km, which is approximately 1.5%, 1.2% and 0.8% for the subregion A, B, and C, respectively. The highest-velocity anomaly observed at the base of the upper mantle in the subregion A is consistent with the differential travel time data shown in Figure 3. The high-velocity structure in Figure 3 is more consistent with a horizontally lying slab, as a penetrating slab would predict a steady velocity increase with depth as low temperatures persist into the lower mantle.

[19] We also found that the averaged amplitude of velocity anomalies above 660 km decreases systematically from subregion A to subregion C. This variation appears to be consistent with the distribution of the subducted lithosphere of the Pacific plate beneath the region imaged by tomographic inversion [e.g., *Fukao et al.*, 1992, 2001]. Figure 9a shows the AB raypaths in the depth range between 600 and 660 km. The P wave velocity perturbations in the depth range of 551–629 km from *Fukao et al.* [2001] are also shown for comparison. In general, there is a good agreement between our velocity models and the tomographic image. A substantial amount of AB raypaths is within the high-velocity zone in the tomographic image, resulting in a higher-than-normal velocity within these depths. The amount of ray segment inside the high-velocity anomalies decreases with increasing azimuth from the subregion A to the subregion C, leading to a gradual decrease in average velocity above the 660 km discontinuity. The high-velocity anomalies shown in the tomographic image is much weaker immediately below the 660 km discontinuity (Figure 9b). It appears that the CD raypaths in the subregion A touch the edge of the anomalies (Figure 9b), and this may explain a

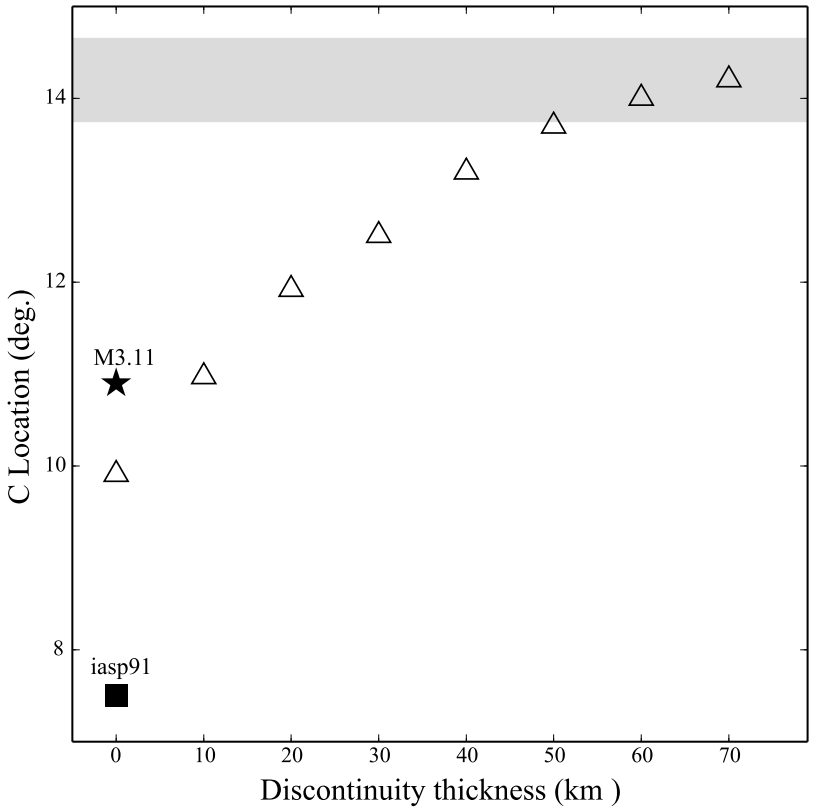

Figure 10. Emerging distance of the C cusp is shown as a function of the discontinuity thickness. The filled region indicates the observed distance range of the C cusp. Also shown are the estimates from the M3.11 and the iasp91 models.

relatively low velocity profile below the 660 km observed for the subregion A (Figure 8d).

[20] All the previous models derived from waveform triplications [e.g., *Tajima and Grand*, 1995; *Wang et al.*, 2006; *Wang and Chen*, 2009] invoked a sharp 660-km discontinuity. Thus, the most surprising feature of our final models is the broad 660-km discontinuity, which has a thickness of ~50–70 km. As discussed above, the broad discontinuity is constrained by the emerging distance of the C cusp. To see how well the discontinuity thickness is constrained, we generated a series models by varying the discontinuity thickness of the subregion A model. Synthetic seismograms at a distance range of 6°–32° were computed, and the emerging distances of the C cusp were picked. We only picked the CD phase whose relative amplitude with respect to the AB phase is greater than the signal-to-noise ratio observed from the data. As shown in Figure 10, the emerging distance of the C cusp increases gradually with the discontinuity thickness. The observed emerging distance of ~14° requires a discontinuity thickness of ~50–70 km. For comparison we also showed the emerging distances of the C cusp estimated from the iasp91 and M3.11 [*Tajima and Grand*, 1995] synthetics. The M3.11 synthetics were further shown with the record section A in Figure 11a. It is clear that the M3.11 synthetics cannot match the CD waveforms in the short distances (before the crossover), although they provide a reasonable fit to the AB waveforms after 22°.

[21] A depressed 660-km discontinuity can also delay the appearance of the CD phase, resulting in a large occurrence distance of the C cusp. However, the amount of delay in the occurring distance of the CD phase requires an unreasonably deep 660-km discontinuity. We extensively searched the models with a sharp and depressed 660-km discontinuity and found that these models cannot provide the desired fitting to the data. Thus, the broad discontinuity observed here must be a robust feature.

[22] *Ito and Takahashi* [1989] found that the pressure interval where ringwoodite and perovskite plus magnesiowüstite coexist is less than 0.1 GPa based on quench experiments. *Hirose* [2002] and *Nishiyama et al.* [2004], on the other hand, observed a relatively wide pressure interval (0.5–0.7 GPa) for the post-spinel transformation in pyrolite. More recently, *Litasov and Ohtani* [2005] confirmed that interval must be narrow (0.1−0.5 GPa) with in situ X-ray diffraction study of anhydrous pyrolite. Based on these results, the 660 km must be a sharp discontinuity with a thickness less than 20 km if it is solely caused by the post-spinel phase transition. Such a sharp discontinuity is consistent with many seismic observations in other regions [e.g., *Vidale and Benz*, 1992]. Laboratory studies also suggested that the post-spinel phase has a negative Clapeyron slope [*Ito and Takahashi*, 1989; *Katsura et al.*, 2003; *Fei et al.*, 2004], which is frequently used to explain the depressed 660-km observed within subduction zones [e.g., *Shearer and Masters*, 1992; *Vidale and Benz*, 1992; *Wicks and Richards*, 1993; *Niu and Kawakatsu*, 1995; *Tajima and Grand*, 1995; *Collier and Helffrich*, 1997; *Flanagan and Shearer*, 1998; *Niu et al.*, 2005; *Li et al.*, 2008]. It is thus almost impossible to

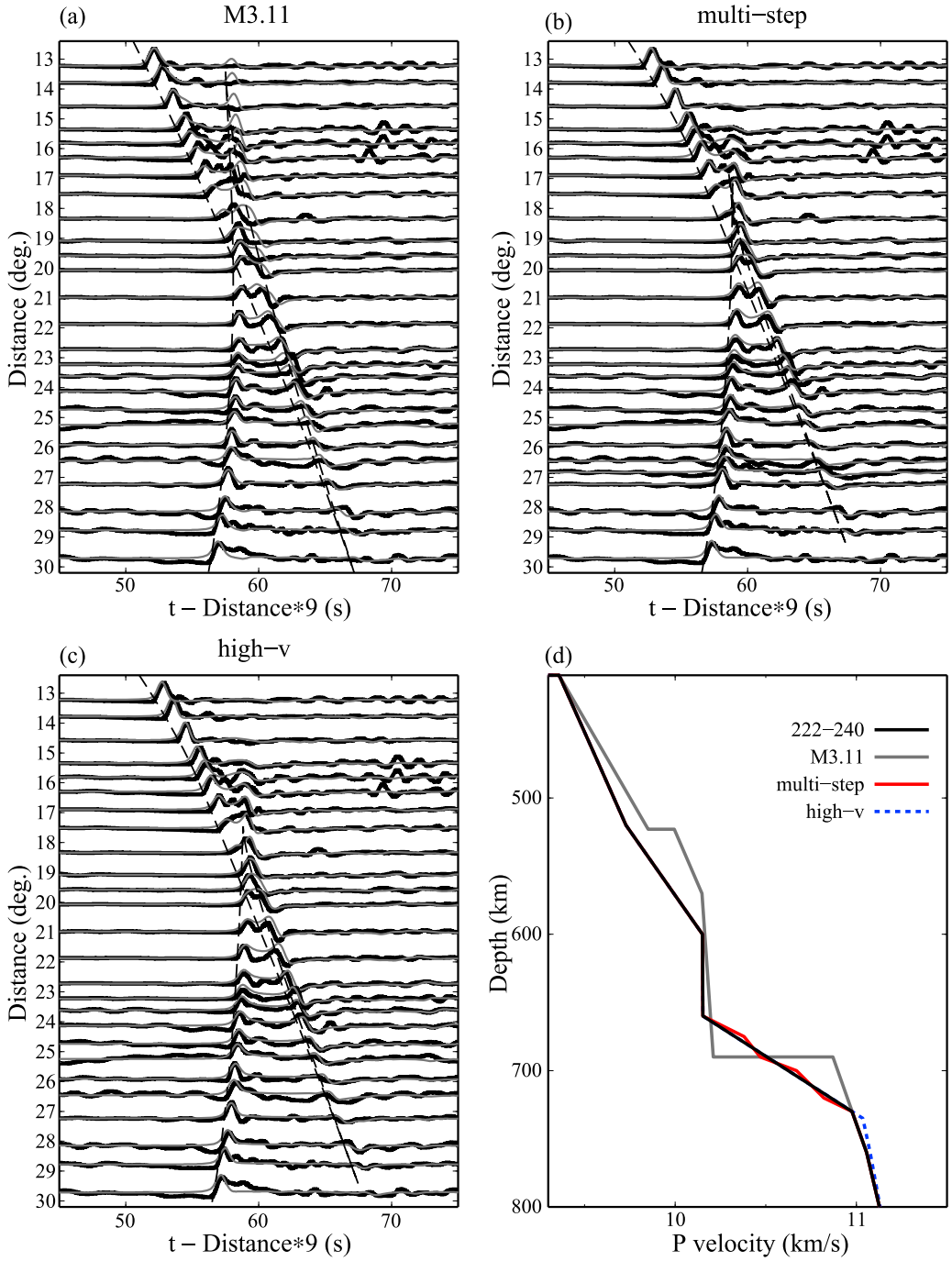

Figure 11. . (a–c) Synthetic seismogram calculated from (d) velocity models. The ray-theory- based travel times calculated from the corresponding velocity model are also plotted.

employ the post-spinel phase transition to explain the gradual boundary observed here, which extends from 660 to 720 km deep.

[23] The transition zone minerals, wadsleyite and ringwoodite, are known to have an enhanced water storage capacity over the upper and lower mantle mineral assemblages [e.g., *Kohlstedt et al.*, 1996]. *Litasov and Ohtani* [2005] measured the Clapeyron slopes of the post-spinel phase transition of the anhydrous and hydrous (1–2 wt% water) ringwoodite and found the latter has a more consistent slope with seismic observations. They further suggested that a significant portion of the seismically observed topography in subduction zones could be caused by water content rather than temperature. The presence of water can delay the post-spinel phase transition, but it does not seem to have a noticeable effect on the pressure interval wherein ringwoodite, perovskite, and magnesiowüstite coexist [*Higo et al.*, 2001; *Litasov and Ohtani*, 2005]. Invoking water in transition zone minerals thus does not seem to work either.

[24] Thus, it is most likely that the broadened 660 km is generated by the dissolution of ringwoodite coupled with a serious phase transformations of the nonolivine minerals.

Vacher et al. [1998] calculated *P*- and *S*-wave velocities with pyrolite and piclogite assemblages and found that in a cold environment transforming majorite garnet to ilmenite and ilmenite to perovskite can generate noticeable steps in the velocity profiles. Multiple seismic discontinuities at a depth of around 660 km were also observed by several receiver-function studies [*Niu and Kawakatsu*, 1996; *Simmons and Gurrola*, 2000; *Ai et al.*, 2003]. The final models shown in Figure 8d thus may simply be a smooth version of velocity profiles with multiple small steps. To test this idea, we calculated the synthetic seismograms (Figure 11b) for a velocity model with three moderate steps (red line in Figure 11d). Each step has a 2% velocity increase within a 10–15 km depth interval. These synthetics can fit the data equally well (Figure 11b), suggesting that the multistep velocity models are good candidates of the true velocity structure beneath the study region. In fact our study region is located very close to the multidiscontinuity area identified by *Ai et al.* [2003] (dashed yellow rectangle in Figure 9). It should be noted that the number of steps is not well constrained by the data. We calculated synthetic seismograms using models with two first-order discontinuities located at 680 and 710 km. The velocity jumps across the two discontinuities were varied from ~1% to 4%, and we found models with a small velocity jump (~1%) provided reasonable fits to the data, whereas those with a large velocity increase (~3%) had large misfits. To summarize the synthetics tests, it seems that our data could not resolve whether the broadened 660 km discontinuity is a layer with constant gradient or consists of multiple layers with low-amplitude velocity jumps. All these models, however, point to a broad 660 km discontinuity in the region.

[25] Our preferred models and the M3.11 model all have a normal velocity below the 660 km discontinuity, which implies no slab penetration into the lower mantle here. To test how well the lower mantle velocity was constrained, we calculated the synthetic seismograms (Figure 11c) for a model that is otherwise similar to the section A model except for a high-velocity anomaly with a peak amplitude of 0.6% extending from 720 to 800 km (blue dashed line in Figure 11d). The high-velocity model does improve the fitting in the distance range of 23°–24°. But the match in the distance range of 20°–23° is significantly deteriorated. Thus, no substantial high-velocity anomalies should be present below the 660 km discontinuity.

5. Conclusions

[26] We investigated the velocity structure around 660 km discontinuity beneath northeast China by modeling more than 650 regional waveforms recorded by the huge CEArray from a deep focus earthquake. The high-quality data set provided a full coverage of the triplication that allowed us to put tight constraints on both radial and lateral variations of the P wave velocity. The triplication also provides strong evidence for a broad 660 km discontinuity extending from 660 to ~720 km deep beneath the study area. This broad discontinuity is likely generated by phase transformations associated with olivine and garnet minerals under low-temperature conditions. The data set also reveals a low-gradient, high-velocity layer immediately above the 660 km discontinuity with some lateral variations that are consistent with tomographic models. Velocity structure below 660 km appears to be normal. The last two observations are consistent with a scenario for subhorizontal subduction.

[27] **Acknowledgments.** Waveform data for this study are provided by Data Management Centre of the China National Seismic Network at Institute of Geophysics, China Earthquake Administration. Discussions with Steve Grand and Elizabeth Vanacore were very helpful in preparing the manuscript. Critical comments from two anonymous reviewers and the Associate Editor significantly improved the quality of this paper. We thank Rongjiang Wang for making his code available to us. This work was supported by NSF grant EAR-063566.

References

Ai, Y., T. Zheng, W. Xu, Y. He, and D. Dong (2003), A complex 660 km discontinuity beneath northeast China, *Earth Planet. Sci. Lett.*, *212*, 63–71, doi:10.1016/S0012-821X(03)00266-8.

Brudzinski, M. R., and W. P. Chen (2000), Variation in P wave speeds and outboard earthquakes, Evidence for a petrologic anomaly in the mantle transition zone, *J. Geophys. Res.*, *105*, 21,661–21,682, doi:10.1029/2000JB900160.

Brudzinski, M. R., and W.-P. Chen (2003), A petrologic anomaly accompanying outboard earthquakes beneath Fiji-Tonga, Corresponding evidence from broadband *P* and *S* waveforms, *J. Geophys. Res.*, *108*(B6), 2299, doi:10.1029/2002JB002012.

Buland, R., and C. H. Chapman (1983), The computation of seismic travel times, *Bull. Seismol. Soc. Am.*, *73*, 1271–1302.

Collier, J., and G. Helffrich (1997), Topography of the "410" and "660" km seismic discontinuities in the Izu-Bonin subduction zone, *Geophys. Res. Lett.*, *24*(12), 1535–1538, doi:10.1029/97GL01383.

Fei, Y., J. Van Orman, J. Li, W. van Westrenen, C. Sanloup, W. Minarik, K. Hirose, T. Komabayashi, M. Walter, and K. Funakoshi (2004), Experimentally determined postspinel transformation boundary in Mg_2SiO_4 using MgO as an internal pressure standard and its geophysical implications, *J. Geophys. Res.*, *109*, B02305, doi:10.1029/2003JB002562.

Flanagan, M., and P. Shearer (1998), Global mapping of topography on transition zone velocity discontinuities by stacking *SS* precursors, *J. Geophys. Res.*, *103*(B2), 2673–2692, doi:10.1029/97JB03212.

Fukao, Y., M. Obayashi, H. Inoue, and M. Nenbai (1992), Subducting slabs stagnant in the mantle transition zone, *J. Geophys. Res.*, *97*(B4), 4809–4822, doi:10.1029/91JB02749.

Fukao, Y., S. Widiyantoro, and M. Obayashi (2001), Stagnant slabs in the upper and lower mantle transition region, *Rev. Geophys.*, *39*, 291–323, doi:10.1029/1999RG000068.

Higo, Y., T. Inoue, T. Irifune, and H. Yurimoto (2001), Effect of water on the spinel-postspinel transformation in Mg2SiO4, *Geophys. Res. Lett.*, *28* (18), 3505–3508, doi:10.1029/2001GL013194.

Hirose, K. (2002), Phase transitions in pyrolitic mantle around 670 km depth: Implications for upwelling of plumes from the lower mantle, *J. Geophys. Res.*, *107*(B4), 2078, doi:10.1029/2001JB000597.

Ito, E., and E. Takahashi (1989), Postspinel transformations in the system Mg_2SiO_4–Fe_2SiO_4 and some geophysical implications, *J. Geophys. Res.*, *94*(B8), 10,637–10,646, doi:10.1029/JB094iB08p10637.

Katsura, T., et al. (2003), Post-spinel transition in Mg_2SiO_4 determined by high *P-T* in situ X-ray diffractometry, *Phys. Earth Planet. Inter.*, *136*, 11–24, doi:10.1016/S0031-9201(03)00019-0.

Kennett, B. L. N., and E. R. Engdahl (1991), Traveltimes for global earthquake location and phase identification, *Geophys. J. Int.*, *105*, 429–465, doi:10.1111/j.1365-246X.1991.tb06724.x.

Kohlstedt, D. L., H. Keppler, and D. C. Rubie (1996), Solubility of water in the α, β and γ phases of $(Mg,Fe)_2SiO_4$, *Contrib. Mineral. Petrol.*, *123*, 345–357, doi:10.1007/s004100050161.

Li, X., and X. Yuan (2003), Receiver functions in northeast China-implications for slab penetration into the lower mantle in northwest Pacific subduction zone, *Earth Planet. Sci. Lett.*, *216*, 679–691, doi:10.1016/S0012-821X(03)00555-7.

Li, J., Q.-F. Chen, E. Vanacore, and F. Niu (2008), Topography of the 660-km discontinuity beneath northeast China: Implications for a retrograde motion of the subducting Pacific slab, *Geophys. Res. Lett.*, *35*, L01302, doi:10.1029/2007GL031658.

Litasov, K. D., and E. Ohtani (2005), Phase relations in hydrous MORB at 18–28 GPa: Implications for heterogeneity of the lower mantle, *Phys. Earth Planet. Inter.*, *150*, 239–263, doi:10.1016/j.pepi.2004.10.010.

Nishiyama, N., T. Irifune, T. Inoue, J. Ando, and K. Funakoshi (2004), Precise determination of phase relations in pyrolite across the 660 km seismic discontinuity by in situ X-ray diffraction and quench experiments,

Phys. Earth Planet. Inter., *143–144*, 185–199, doi:10.1016/j.pepi.2003.08.010.

Niu, F., and H. Kawakatsu (1995), Direct evidence for the undulation of the 660-km discontinuity beneath Tonga: Comparison of Japan and California array data, *Geophys. Res. Lett.*, *22*(5), 531–534, doi:10.1029/94GL03332.

Niu, F., and H. Kawakatsu (1996), Complex structure of mantle discontinuities at the tip of the subducting slab beneath Northeast China-A preliminary investigation of broadband receiver functions, *J. Phys. Earth*, *44*, 701–711.

Niu, F., A. Levander, S. Ham, and M. Obayashi (2005), Mapping the subducting Pacific slab beneath southwest Japan with Hi-net receiver functions, *Earth Planet. Sci. Lett.*, *239*, 9–17, doi:10.1016/j.epsl.2005.08.009.

Shearer, P. M., and T. G. Masters (1992), Global mapping of topography on the 660-km discontinuity, *Nature*, *355*, 791–796, doi:10.1038/355791a0.

Simmons, N. A., and H. Gurrola (2000), Multiple seismic discontinuities near the base of the transition zone in the Earth's mantle, *Nature*, *405*, 559–562, doi:10.1038/35014589.

Tajima, F., and S. P. Grand (1995), Evidence of high velocity anomalies in the transition zone associated with Southern Kurile Subduction Zone, *Geophys. Res. Lett.*, *22*(23), 3139–3142, doi:10.1029/95GL03314.

Tajima, F., and S. P. Grand (1998), Variation of transition zone high-velocity anomalies and depression of 660 km discontinuity associated with subduction zones from the southern Kuriles to Izu-Bonin and Ryukyu, *J. Geophys. Res.*, *103*(B7), 15,015–15,036, doi:10.1029/98JB00752.

Vacher, P., A. Mocquet, and C. Sotin (1998), Computation of seismic profiles from mineral physics: The importance of the non-olivine components for explaining the 660 km depth discontinuity, *Phys. Earth Planet. Inter.*, *106*, 275–298, doi:10.1016/S0031-9201(98)00076-4.

Vidale, J. E., and H. M. Benz (1992), Upper-mantle seismic discontinuities and the thermal structure of subduction zones, *Nature*, *356*, 678–683, doi:10.1038/356678a0.

Wang, R. (1999), A Simple orthonormalization method for stable and efficient computation of Green's functions, *Bull. Seismol. Soc. Am.*, *89*, 733–741.

Wang, T., and L. Chen (2009), Distinct velocity variations around the base of the upper mantle beneath northeast Asia, *Phys. Earth Planet. Inter.*, *172*, 241–256, doi:10.1016/j.pepi.2008.09.021.

Wang, Y., L. Wen, D. Weidner, and Y. He (2006), *SH* velocity and compositional models near the 660-km discontinuity beneath South America and northeast Asia, *J. Geophys. Res.*, *111*, B07305, doi:10.1029/2005JB003849.

Wicks, C. W., Jr., and M. A. Richards (1993), A detailed map of the 660-kilometer discontinuity beneath the Izu-Bonin subduction zone, *Science*, *261*, 1424–1427, doi:10.1126/science.261.5127.1424.

Zheng, X.-F., B. Ouyang, D.-N. Zhang, Z.-X. Yao, J. H. Liang, and J. Zheng (2009), Technical system construction of Data Backup Centre for China Seismograph Network and the data support to researches on the Wenchuan earthquake (in Chinese), *Chin. J. Geophys.*, *52*, 1412–1417, doi:10.3969/j.issn.0001-5733.

F. Niu and B. Wang, Department of Earth Science, Rice University, 6100 Main St., Houston, TX 77005, USA. (wangbs@cea-igp.ac.cn)